Defect generation in polymer-bonded explosives exposed to internal gas injection $\ensuremath{ igoplus }$

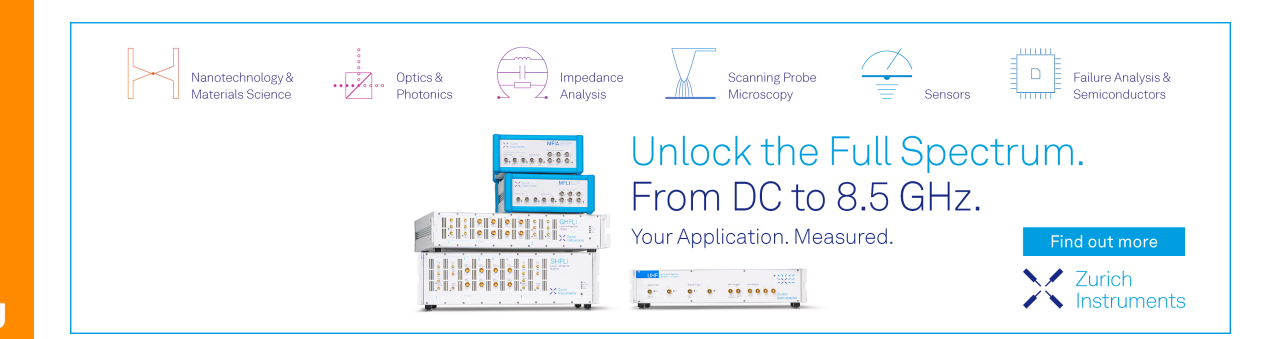
Levi Kirby; Travis Sippel [®]; H. S. Udaykumar [®]; Xuan Song ■ [®]



J. Appl. Phys. 134, 155101 (2023) https://doi.org/10.1063/5.0172427









Defect generation in polymer-bonded explosives exposed to internal gas injection

Cite as: J. Appl. Phys. 134, 155101 (2023); doi: 10.1063/5.0172427 Submitted: 15 August 2023 · Accepted: 30 September 2023 · Published Online: 16 October 2023







Levi Kirby,¹ Travis Sippel,² D H. S. Udaykumar,³ D and Xuan Song^{1,3,a)} D



AFFILIATIONS

- ¹Department of Industrial and Systems Engineering, The University of Iowa, Iowa City, Iowa 52242, USA
- ²Department of Mechanical and Aerospace Engineering, University of Missouri, Columbia, Missouri 65201, USA
- ³Department of Mechanical Engineering, The University of Iowa, Iowa City, Iowa 52242, USA

ABSTRACT

Sensitivity in polymer-bonded explosives (PBXs) relies on the presence of defects, such as cracks and voids, which create localized thermal energy, commonly known as hotspots, and initiate reactions through various localization phenomena. Our prior research has explored the use of internal gas pressure induced by thermite ignition to generate localized defects for PBX sensitization. However, further research is required to gain a more comprehensive understanding of the defect generation process resulting from internal gas pressure. This study & investigates the process of defect generation in PBXs in response to internally induced gas pressure by applying controlled compressed gas 🖁 employed to visualize the microstructure of the sample before and after gas injection. The experiments reveal the significance of gas pressure, cavity shape, temperature, and specimen compaction pressure in the defect generation. were conducted to assess the defect generation in mock PBXs under varying gas pressures, cohesive properties, and binder thicknesses. The simulation results demonstrate the substantial influence of these properties on the ability to generate defects in mock PBXs. This study contributes to a better understanding of the factors influencing defect generation in mock PBXs. This knowledge is crucial for achieving precise $\bar{\sigma}$ control over defect generation, leading to improved ignition and detonation characteristics in PBXs.

Published under an exclusive license by AIP Publishing. https://doi.org/10.1063/5.0172427

I. INTRODUCTION

Polymer-bonded explosives (PBXs) are a class of energetic materials consisting of energetic crystals bonded together with a polymer binder.1 These materials usually exhibit microstructural defects, such as cracks and voids, which can lead to the formation of hotspots and initiate reactions through various localization phenomena such as void collapse.²⁻⁴ This, in turn, enhances the ignition threshold, shock sensitivity, and detonation characteristics of PBXs.⁵⁻⁹ While much of the research has highlighted defects within crystals as the primary causes of PBX sensitivity, 10 some experimental and theoretical evidence has shown defects within the non-crystal phase, particularly at the particle/binder interface, can also be influential. 4,11,12 However, from a standpoint of safety,9 all these defects and the resulting increased sensitivity are undesirable for PBXs during manufacture, storage, and transport. Effective control of these defects for specific working environments holds the promise of optimizing PBX performance and ensuring safety across their applications.

In recent years, there has been growing interest in the development of "switchable" explosives, ^{13–16} which exhibit insensitivity to unintended stimuli but can switch to high performance during use. In our prior work, 17,18 we proposed to utilize internally induced gas pressure in PBXs to generate localized defects for PBX sensitization. This gas pressure, for example, can be induced through thermite ignition upon microwave illumination, as depicted in Figs. 1(a)-1(c). The objective of this study is to investigate the process of defect generation in PBXs in response to internally induced gas pressure. To simulate the release of gas exhausts inside PBXs resulting from thermite ignition, controlled-pressure nitrogen gas was injected into custom-made cavities within cast mock PBX samples. The microstructures of the samples were examined using x-ray micro-computed tomography (micro-CT) before and after the injection of the nitrogen gas. This allows for a detailed analysis

a) Author to whom correspondence should be addressed: xuan-song@uiowa.edu

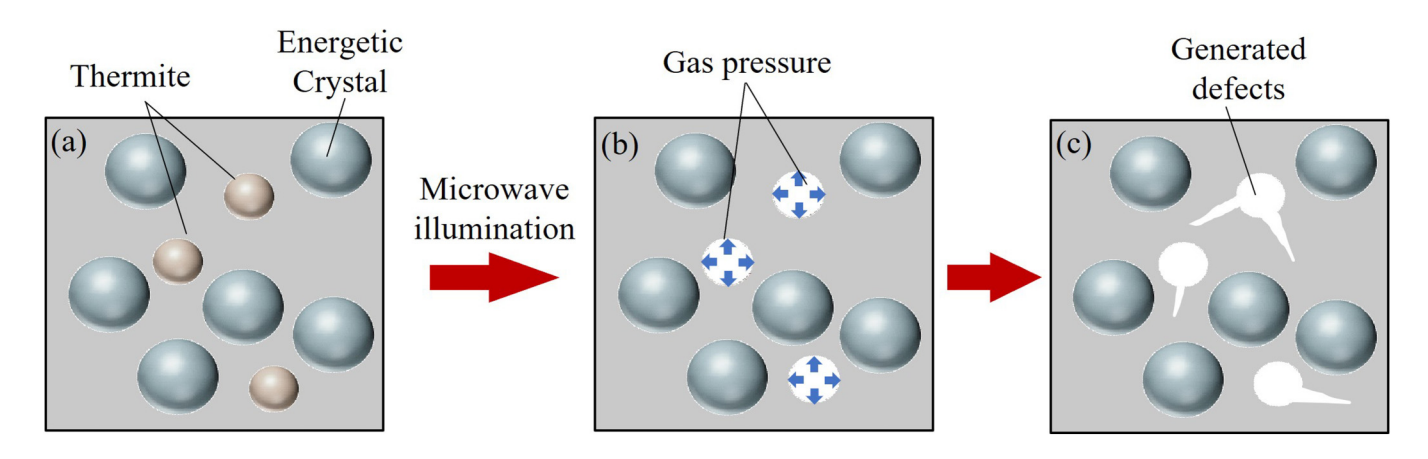


FIG. 1. Our prior research in controlling the presence of defects in PBX through microwave-induced gas pressure. (a) A PBX containing thermites. (b) Internally induced gas pressure upon microwave illumination. (c) Defects generated by the internal gas pressure.

of the defect generation process under varying conditions, including gas pressure, cavity geometry, temperature, and compaction pressure for sample fabrication. In addition to experimental analysis, numerical simulations were conducted to gain in-depth understanding of the defect generation mechanism through exploring the influence of various factors, such as binder thickness and interface

The rest of the paper is organized as follows. Section II outlines the experimental methods employed to fabricate mock PBX samples with internal cavities, as well as the procedures for injecting gas into the cavities. Additionally, a defect characterization method utilizing micro-CT is introduced, along with a detailed description of the finite element analysis (FEA) conducted. Section III presents the results of the micro-CT analysis and the FEA.

II. METHODS

A. Materials

Due to safety concerns, sucrose was selected as a surrogate (mock) material in this study due to its similar morphology and mechanical behavior to real explosive crystals.¹⁹ A hydroxylterminated polybutadiene (HTPB) binder developed in our previous work²⁰ was used, which consists of 75.25 wt. % HTPB monomer (R45M, RCS), 1.43 wt. % tepanol bonding agent (HX-752, RCS), 15.05 wt. % plasticizer (isodecyl pelargonate or IDP, RCS), and 8.27 wt. % curative (isophorone diisocyanate or IPDI from Sigma Aldrich). This binder demonstrates excellent reproducibility, satisfactory mechanical properties, reduced sensitivity to temperature and aging effects, and ease of curing.²

B. Sample fabrication

A die pressing approach was utilized to fabricate cast mock PBXs with different internal cavities, such as cube, cone, and sphere, as depicted in Fig. 2(a). Sucrose powder and HTPB binders were manually mixed at a fixed solids ratio of 80 wt. % and loaded in a press die. A cavity punch with a specific convex pattern

[Fig. 2(b)] was printed by fused deposition modeling and inserted into the die before a top punch was loaded to compress the mixture at a given compaction pressure (0, 10, and 20 MPa). This formed a composite (bottom part) with a cavity feature defined by the cavity punch, as shown in Fig. 2(c). To seal off the cavity, a composite cap (top part) without a cavity was fabricated in a similar manner and combined with the bottom part. A light layer of binder and sucrose particles were applied between the two comof binder and sucrose particles were applied between the two composite parts to ensure an airtight bond at the interface [Fig. 2(g)]. The two-part composite was cured together at 60 °C for one week, leading to a solid mock PBX with a precise internal cavity. Table I sits different parameter levels used in the sample fabrication, including cavity geometry (cube, cone, and sphere) and compaction $\frac{\vec{n}}{N}$ pressure (0, 10, and 20 MPa).

To achieve gas injection into the internal cavity, a 25G Luer-Lok stainless-steel needle was inserted through a precisely drilled hole in the top cap of the mock PBX. Since the stainlesssteel needle can cause artifacts during micro-CT scanning, it needs to be removed prior to scanning. To facilitate the easy removal of the Luer-Lok needle from the sample, the needle was slid through PEEK tubing, which was then inserted into the cavity. The sleeve was securely attached to the needle and glued to the top cap of the mock PBX, creating a sealed pressure aperture that could be detached if required. The assembly process is illustrated in Fig. 2(d). The final configuration of the sample for gas injection is depicted in Figs. 2(e) and 2(f).

C. Gas injection

The experimental setup for gas injection is depicted in Figs. 3(a) and 3(b). The gas was supplied by a 75 L nitrogen tank equipped with a pressure regulator. The pressure regulator allowed for precise control of the output pressure within the range of 0-7 MPa. The gas was transmitted from the pressure regulator to a high-pressure gas valve through high-pressure tubing. From the gas valve, the gas was then directed to the Luer-Lok needle attached to the sample. A pressure gauge was installed between the pressure regulator and the

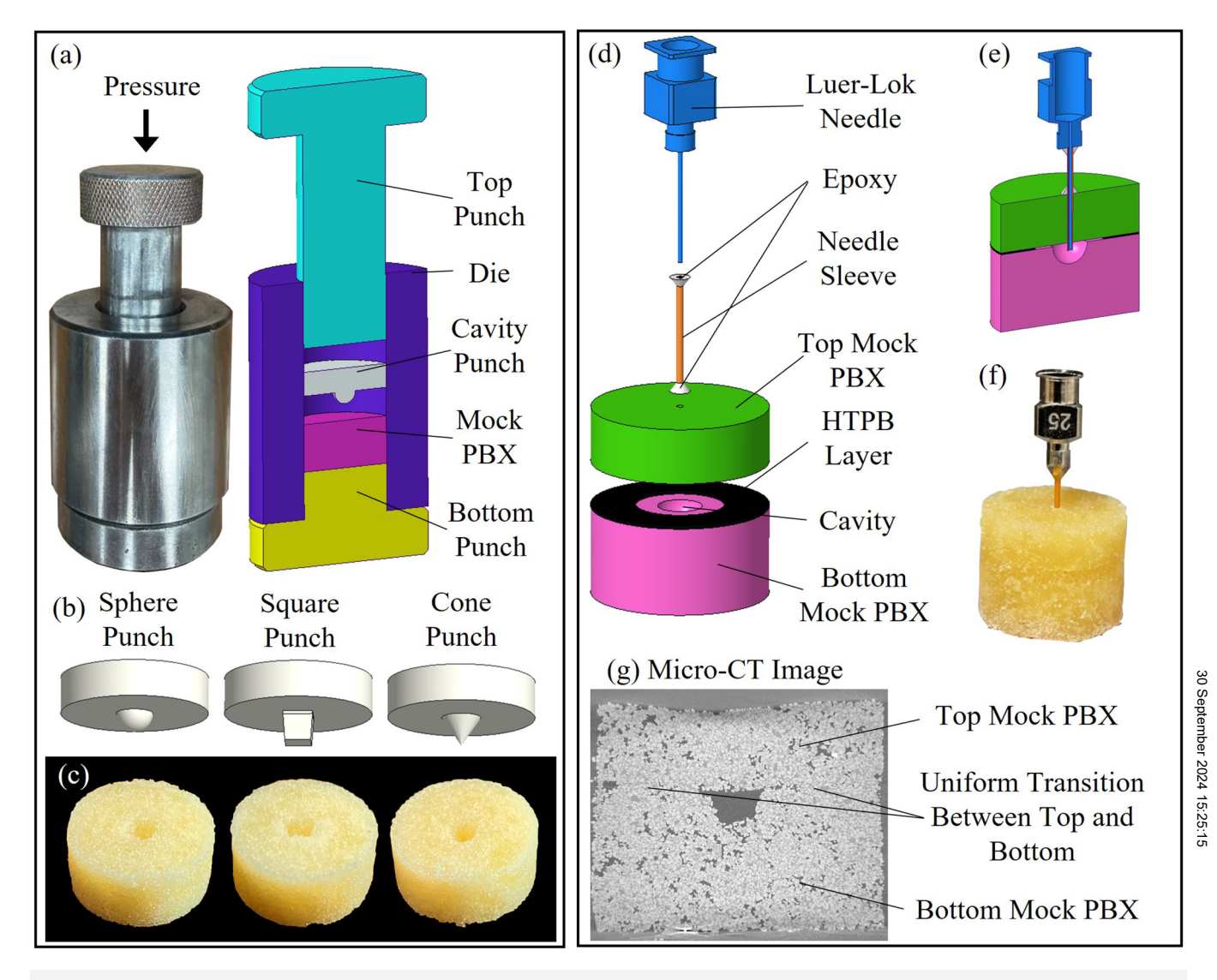


FIG. 2. (a) Die used for cavity creation; (b) cavity punch; (c) final parts with created cavities; (d)–(f) gas application through a nozzle with the final part. (g) The final part with no clear boundary between top and bottom half.

gas valve to monitor the gas pressure during the experiments. The Luer-Lok needle was securely fixed in place using a set screw to ensure the stability of the setup and prevent any external interference, as shown in Fig. 3(c).

In our experiments, an initial micro-CT scan of the sample was performed to establish a baseline for the study of microstructures. The same sample was subsequently heated in an oven for 10 min at temperatures similar to those experienced during thermite ignition (e.g., $200-400\,^{\circ}\text{C}$). Afterward, the sample was immediately secured in the setup and attached to the gas supply. The valve on the gas tank was opened, and the pressure regulator was adjusted to a desired pressure within the range of 0–7 MPa.

Once the pressure was confirmed on the pressure gauge, the gas valve was opened for a duration of 5 s before being closed again. Lastly, the sample was removed from the locking device, and a second micro-CT scan was conducted for comparison. Table I lists different parameter levels used in the gas injection, including gas pressure (4.13, 5.51, and 6.89 MPa) and temperature (170, 200, and 230 °C).

D. Micro-CT

To visualize and quantify the microstructures of the printed specimens, a micro-CT technique was employed using a Zeiss

TABLE I. Different parameter combinations used in our experiments.

Sample	Temperature (deg)	Geometry	Gas pressure (MPa)	Compaction pressure (MPa)
1	230	Cube	5.17	5
2	230	Cone	5.17	5
3	230	Sphere	3.45	5
4	230	Cube	5.17	5
5	230	Cube	6.9	5
6	230	Cube	3.45	0
7	230	Cube	5.17	0
8	230	Cube	6.9	0
9	230	Cube	3.45	10
10	230	Cube	5.17	10
11	230	Cube	6.9	10
12	170	Cube	3.45	5
13	170	Cube	5.17	5
14	170	Cube	6.9	5
15	200	Cube	3.45	5
16	200	Cube	5.17	5
17	200	Cube	6.9	5

Xradia 520 Versa 3D x-ray microscope. The x-ray source voltage was set to $80 \, \text{kV}$ with a power of 7 W. Each projection had an exposure time of 1 s, and a total of 1601 projections were captured over a 360° rotation. Image acquisition was performed using a $0.4\times$ objective, and the distance between the x-ray source and the sample was set at $43 \, \text{mm}$, resulting in a pixel size of $20 \, \mu \text{m}$.

Following the scanning process, the obtained data were reconstructed into DICOM images, which were then imported into Dragonfly software (Object Research Systems). This software provides the necessary tools to differentiate and isolate porosity, sucrose particles, and HTPB binder by leveraging the contrasting density within each sample, as depicted in Fig. 4. Figures 4(a) and 4(d) illustrate the original micro-CT images before and after gas injection, respectively. The particles and binder are highlighted in Figs. 4(b) and 4(e), with a contrast range of 3500–4500 for the binder and 4500–60 000 for the particles. The contrast range for porosity was set from 0 to 3500, as demonstrated in Figs. 4(c) and 4(f). By comparing the porosity before and after gas injection, we can determine key quantities associated with the process of defect generation, such as cavity expansion and change in void volume.

E. Finite element analysis

1. Constituent level

Finite element analysis was employed to validate and investigate the process of defect generation in a cast mock PBX subjected to internal gas injection. The first step involved experimental characterization of our custom binder. The uncured binder was placed in a dog bone mold with dimensions of $10 \times 8 \times 30 \, \text{mm}^3$ and cured for one week at $60 \, ^{\circ}\text{C}$. Subsequently, the cured binder sample

[Fig. 5(a)] was subjected to heating at 230 °C for 10 min, which corresponded to the temperature selected for the gas injection experiments. Tensile tests were then performed using a universal testing machine (TestResources, Shakopee, MN, USA) at a rate of 20 mm/min. The loading curves obtained from the tensile tests were used to extract various material parameters, including elastic parameters (Young's modulus and Poisson's ratio), plastic parameters (yield stress and plastic strain), ductile damage parameters (fracture strain and stress triaxiality), and damage evolution (displacement at failure). The cross-sectional areas of the sample were measured before the tensile testing and at the yield point to calculate longitudinal and lateral strain, which were then used to calculate Poisson's ratio and fracture strain. The stress triaxiality was set at 1/3, as defined in uniaxial tension of ductile materials. ²² Finally, the strain data were utilized to determine the displacement at failure. Final calculations were gathered by taking an average of three replicates.

To verify the material properties, a tensile test simulation was conducted using Abaqus/Standard, as shown in Figs. 5(a)-5(c). The material properties obtained from the tensile test were incorporated in the simulation, including the elastic, plastic, ductile damage, and damage evolution parameters. The lower portion of the simulated sample was set with the encastre boundary condition (BC), while the upper portion was assigned a U2 displacement of 10 mm to simulate tension [Fig. 5(b)]. Element deletion was activated during the meshing procedure to accurately capture polymer damage. This feature ensures that elements exceeding the maximum threshold for displacement to failure were deleted, simulating the breaking of the binder at yield. The element size was experience with the yield point by multiplying the displacement at failure by the element size of 0.15 mm, providing the displacement at failure value used in the simulation. The mesh used a quad structured technique with a size set at 0.5 mm, as shown in 👼 Fig. 5(c). The simulation results were compared with the experimental test data to ensure their validity before extending the analysis to the simulation at the composite level. The material properties for the sucrose particles were set based off parameters found in the literature including Young's modulus and Poisson's

2. Composite level

The simulation at the composite level was conducted in a domain with a cube shape $(20 \times 20 \text{ mm})$. This domain was set as the binder matrix of a mock PBX. A void was created in the center of the matrix with a radius ranging from 1.5 to 2.2 mm. Eighteen sucrose particles were modeled using irregular shapes ranging from 4 to 20 mm^2 and randomly placed within the binder matrix, as depicted in Fig. 5(d). The particle size replicated that of particles found using microscopic imaging. In this study, all simulations employed an identical shape and distribution of sucrose particles.

The particle-binder interface was set using a cohesive model based on values found in previous literature. ^{24,25} The cohesive properties determine the damage experienced by a particle and the surrounding matrix, as described by the Dugdale and Barenblatt models. ^{26,27} A commonly used bilinear traction separation law was

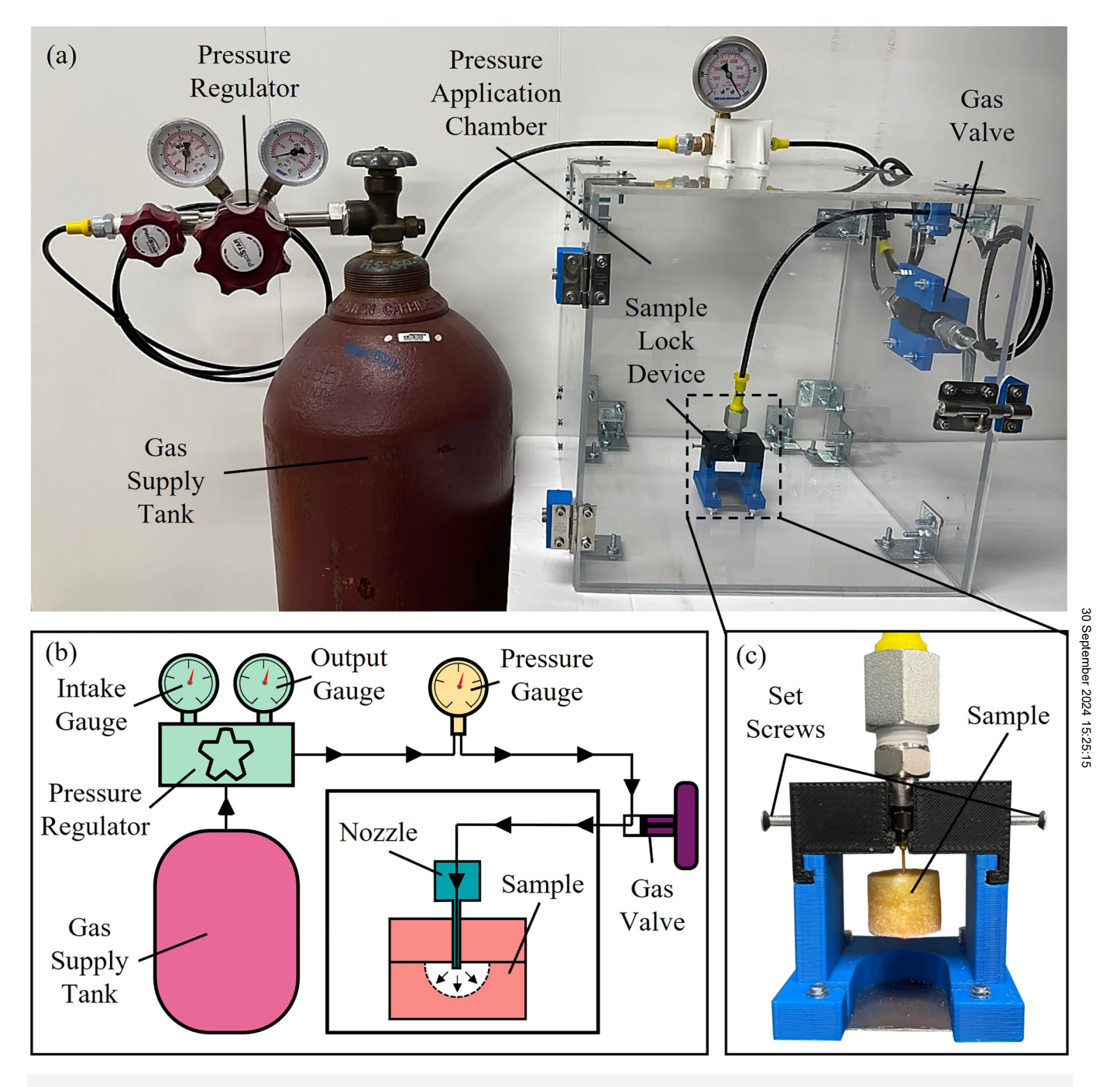


FIG. 3. (a) Experimental setup for gas injection; (b) schematic of gas flow; (c) the sample locking device.

implemented to define the interface behavior. ²⁸ Figure 5(f) illustrates the law, which consists of the initial stiffness ($K_{\rm eff}$), the fracture energy (G_c), the maximum traction (t_n/t_s) at which damage initiation occurs, and the ultimate separation (δ_n/δ_s) at which the cohesive element completely fails, losing its ability to resist shear or

tensile traction. ²⁴ In Abaqus/Standard, the bilinear traction separation law is defined by G_c and K_{eff} , while K_{eff} is broken down into K_{nn} and K_{ss}/K_{tt} , which represent the original un-damaged transverse normal modulus and the original un-damaged transverse shear moduli, respectively. ²⁴

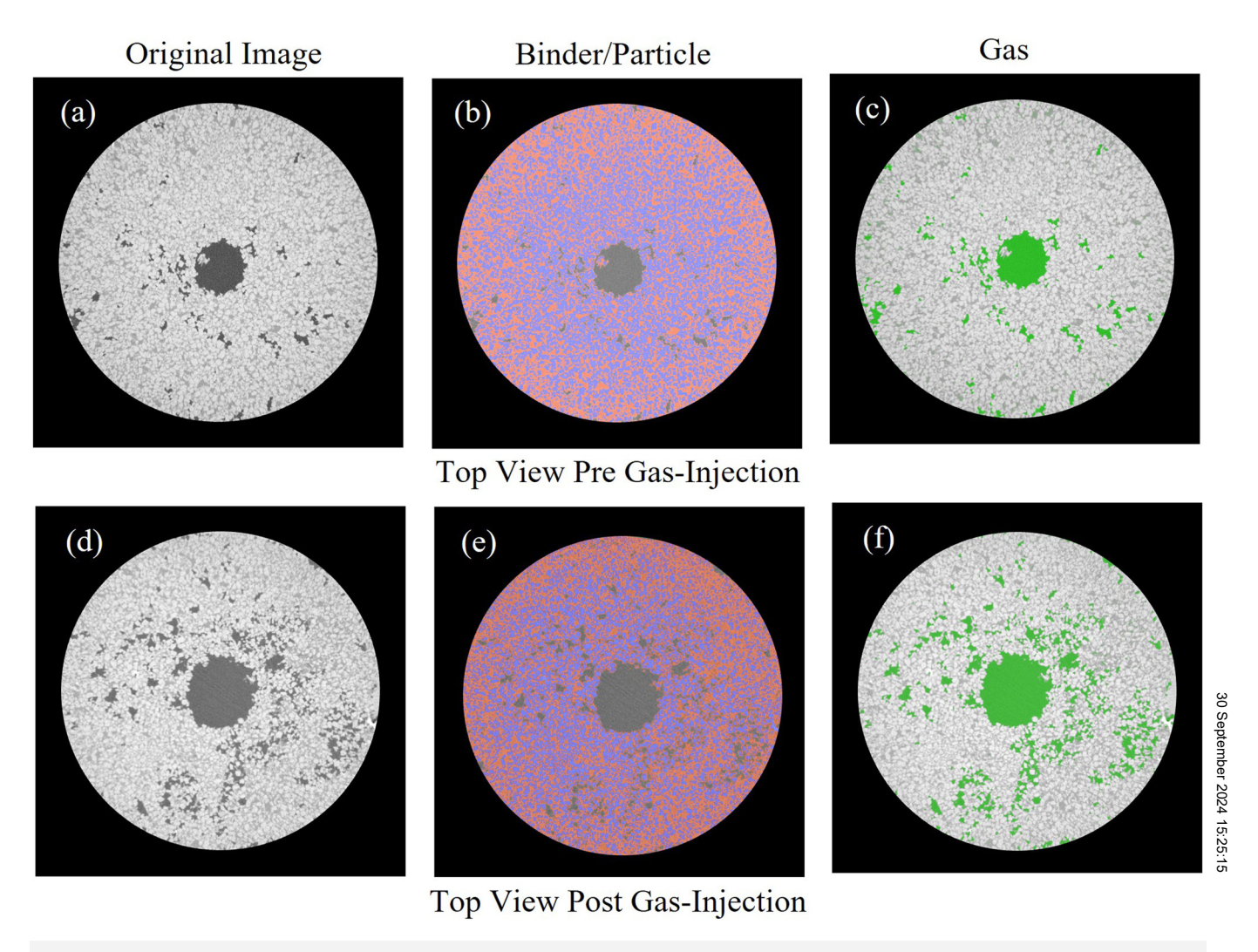


FIG. 4. Micro-CT scans. (a) The scanned image, (b) the binder and particles, and (c) the porous phase before gas injection. (d)–(f) The same phases post gas injection.

The traction–separation law can be expressed by the following: 21,25

$$\begin{cases} t_n = (1-D)\frac{\delta_n}{\delta_{no}} t_{no}, \\ t_s = (1-D)\frac{\delta_s}{\delta_{So}} t_{So}, \end{cases}$$
 (1)

where subscript "n" and "s" represent the normal and the shear direction and the damage factor (D) is defined as the following:

$$D = \begin{cases} 0 & (\delta < \delta_0), \\ \frac{\delta_f(\delta - 0)}{\delta(\delta_f - \delta_0)} & (\delta > \delta_0). \end{cases}$$
 (2)

Damage initiation is expressed by the maximum stress criterion defined below:

$$\max\left(\frac{\langle t_n \rangle}{t_{no}}, \frac{\langle t_s \rangle}{t_{so}}\right) = 1. \tag{3}$$

The values used in the simulation are presented in Table II. The gas pressure was modeled by applying outward pressure to the wall of the cavity. The BC of the lower portion of the composite was set as encastre to prevent any movement. This was a simplification of the experimental setup, where one end of a composite was fixed onto the nozzle [Fig. 3(c)]. The particles were meshed using a quad element with a size of 0.45 mm, while the binder was meshed as quad-free elements with a size of 0.15 mm, as illustrated in Fig. 5(e). Element deletion was also employed to simulate binder

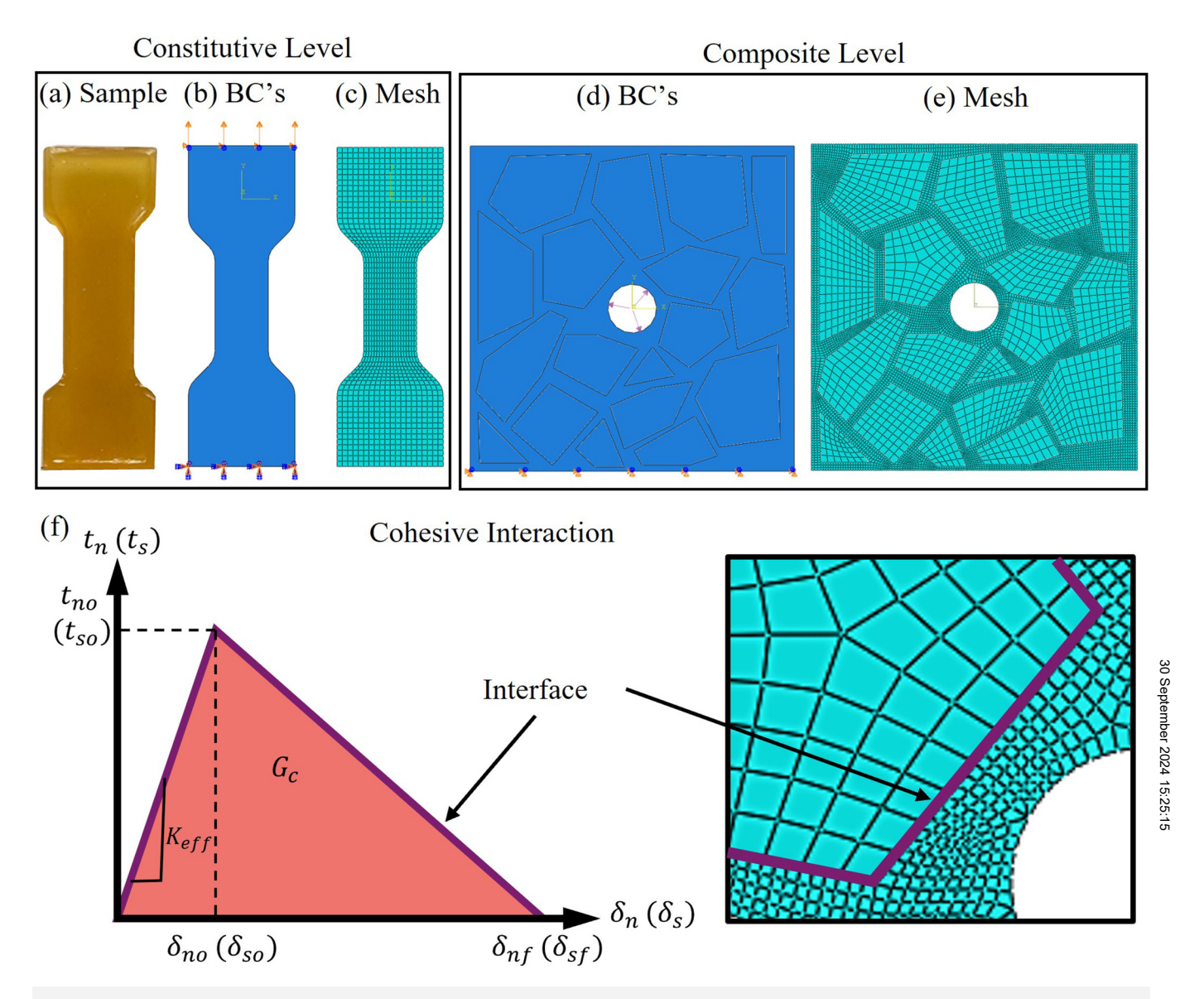


FIG. 5. (a)–(c) A sample and FEA for the constitutive binder. Boundary conditions (BC's) include encastre and displacement in the U2 direction. (d) and (e) FEA for the PBX composite. BC's include encastre and outward force on the inner cavity. (f) Cohesive interaction properties include the initial stiffness (K_{eff}), the fracture energy (G_c), the maximum traction (t_n/t_s) at which damage initiation occurs, and the ultimate separation (δ_n/δ_s) at which the cohesive element completely fails.

TABLE II. Particle and interface properties used in simulation from literature studies (Refs. 20–22).

Particle properties				
Young's modulus (MPa): 31 500	Poisson's ratio: 0.3			
Interaction properties				
Friction coefficient: 0.5	Cohesive behavior: $K_{nn} = 500$,			
	$K_{tt}/K_{ss} = 400$			
Damage: $T_n/T_t = 0.5$	Evolution Parameter: 0.003			

failure, taking into consideration the displacement at failure and the element size.

In the simulation, three properties were investigated in relation to defect generation, including gas pressure, cohesion properties of the composite interface, and the binder thickness around the cavity. For gas pressure, four levels were simulated, including 1, 5, 7, and 7.5 MPa. For cohesion properties, five levels were selected, including $K_{nn}=50,\,K_{ss}/K_{tt}=40;\,K_{nn}=150,\,K_{ss}/K_{tt}=120;\,K_{nn}=200,\,K_{ss}/K_{tt}=160;\,K_{nn}=500,\,K_{ss}/K_{tt}=400;$ and $K_{nn}=1000,\,K_{ss}/K_{tt}=800.$

These values represent the stiffness and strength of the cohesive interaction between the binder and particles, affecting the likelihood of binder delamination and subsequent fracture. For binder thickness, three levels were chosen, including 0.04, 0.12, and 0.36 mm. The higher binder thickness corresponds to a lower solids loading in the mock PBX.

F. Statistical analysis

The obtained experimental data were analyzed in statistical software Minitab²⁹ using Analysis of Variance (ANOVA) to assess significance of the effects of the process parameters on the printed explosives. The p-value for significance of each parameter was calculated, which is defined as the mean of an assumed probability distribution being greater than or equal to the observed results.³⁰ Before performing the ANOVA, the assumptions of normality, independence, and homogeneity of variances were checked.

III. RESULTS AND DISCUSSION

A. Defect classification

Figures 6(a)-6(c) demonstrate the micro-CT images of a specimen before and after the injection of gas. The gas

injection resulted in two types of changes in the microstructures surrounding the internal cavity, including cavity expansion and crack propagation. As shown in Fig. 6(d), upon gas injection, the cavity first underwent a nearly uniform expansion; meanwhile, cracks initiated at specific sites along the cavity wall and propagated toward the outer surface of the sample. Both cavity expansion and crack propagation contributed to an increase in the porosity inside the sample. In this paper, cavity expansion was calculated as the difference in the cavity volume before and after gas injection over the initial cavity volume before gas injection; crack propagation was characterized by the volume of cracks resulting from gas injection; porosity change was calculated as the difference in the specimen porosity before and after gas injection over the initial specimen porosity before gas injection.

B. Influence of gas pressure

The micro-CT scans shown in Figs. 7(a)-7(f) showcase the microstructures of the samples before and after the injection of gas at different pressures into the cavity. It is important to note that the scans were not taken at the exact same location or orientation.

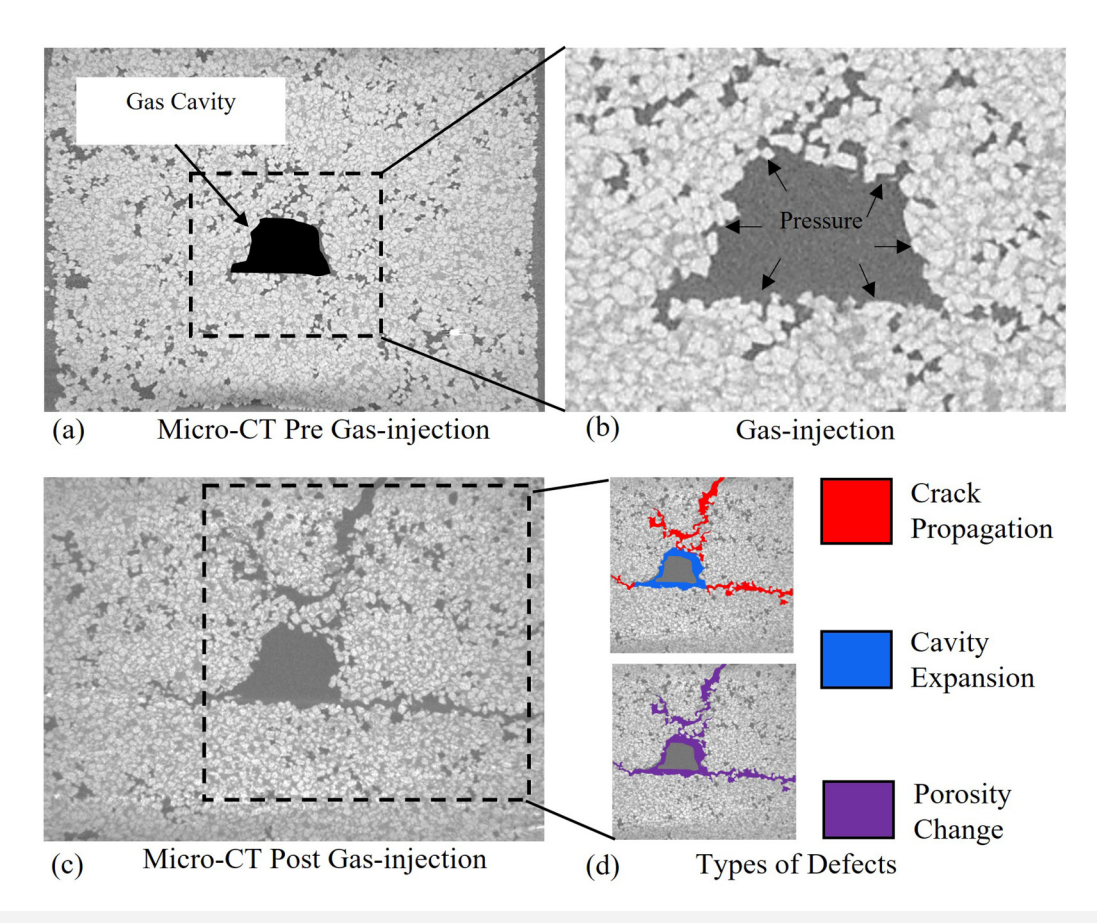


FIG. 6. Micro-CT image of a mock PBX (a), (b) before gas injection and (c) after gas injection. (d) Distinct types of defects generated around the cavity.

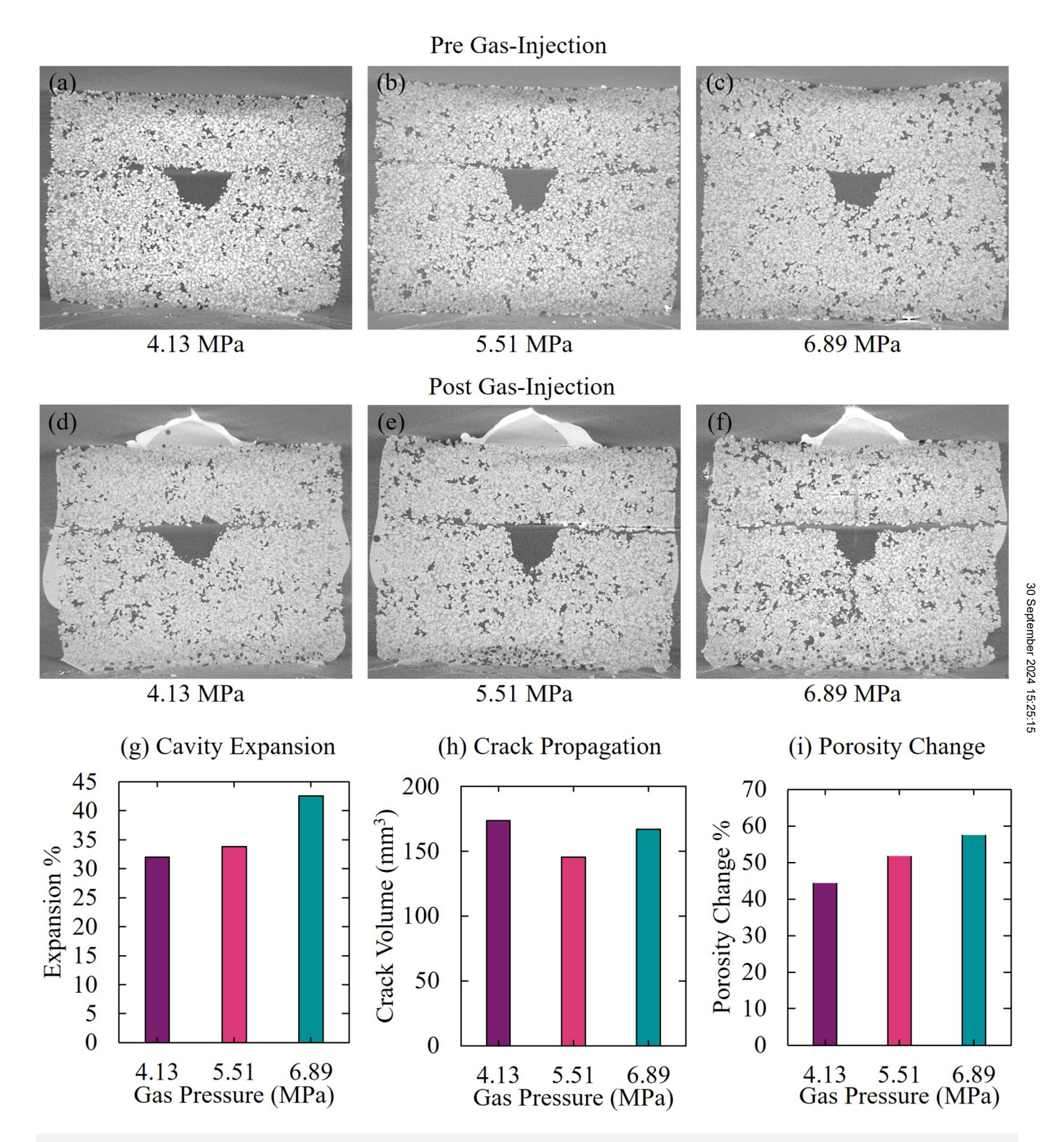


FIG. 7. Micro-CT scans of samples (a)–(c) before gas injection and (d)–(f) after gas injection. Effect of gas pressure on (g) cavity expansion, (h) crack propagation, and (i) porosity change.

Nevertheless, a comparison of these images still reveals valuable insights into the effect of gas pressure on the generated defects. The comparisons reveal that at lower pressures, the crack defects tended to concentrate primarily at the corners of the cavities. In contrast, under the highest pressure, cracks started propagating outward throughout the sample.

Figures 7(g)-7(i) illustrate the influence of gas pressure on cavity expansion, crack propagation, and porosity change in the mock PBX samples. The results indicated that higher pressure led to greater cavity expansion [Fig. 7(g)] and porosity change [Fig. 7(i)], highlighting the critical role of gas pressure as the key driving force behind defect generation. For example, as the gas pressure increased from 4.13 to 6.89 MPa, the cavity expansion increased from 32.03% to 42.5%, and the porosity change increased from 44.6% to 57.7%. The ANOVA further confirmed the significant impact of gas pressure on both cavity expansion (p-value = 0.008) and porosity change (p-value = 0.001). The gas pressure, however, showed no significance on the crack propagation (p-value = 0.330), as suggested by Fig. 7(h). These findings demonstrate that by adjusting the amount of gas emitted by the thermite, it is possible to control the degree of cavity expansion and porosity change within the composite.

C. Influence of cavity geometry

Figures 8(a)-8(f) show the microstructures of samples with varying cavity geometries before and after the injection of gas. It can be seen that the cube [Figs. 8(a) and 8(d)] and the cone cavity [Figs. 8(b) and 8(e)] induced localized crack propagation primarily at their corners due to higher stress concentration. These findings suggest that the cone and cube shapes may have specific applications where location-specific crack propagation is desired.

Figures 8(g)-8(i) depict the influence of cavity geometry on cavity expansion, crack propagation, and porosity change. The ANOVA reveals that cavity shape had a significant effect on cavity expansion (p-value = 0.002) and porosity change (p-value = 0.000) and exhibited a less significant effect on crack propagation (p-value = 0.097). It was observed that the sphere cavity resulted in almost the highest cavity expansion, crack propagation, and porosity change, while the cone shape exhibited the lowest cavity expansion, crack propagation, and porosity change. The cube cavity led to cavity expansion similar to the cone cavity and resulted in higher crack propagation compared to the other two geometries. The high cavity expansion resulting from the sphere cavity can be attributed to its ability to distribute stress more uniformly when the gas was injected, facilitating the cavity expansion and delaying cracking. In contrast, the cone and cube shapes experienced stress concentration at the corners, resulting in cracking before significant expansion could take place. The results indicate that the sphere shape is the most suitable for maximizing cavity expansion and porosity change. Considering the overall performance and potential applications, the sphere cavity was selected for all simulation tests due to its ability to achieve maximum expansion and porosity change.

D. Influence of temperature

Figures 9(a)-9(f) illustrate the impact of temperature on the microstructures of samples. It is observed that at lower temperatures, the defects tended to concentrate at the corners of the composite as indicated by the red arrows in Fig. 9(e). In contrast, at the highest temperature, cracking was more evenly distributed throughout the composite, indicated by the red arrow in Fig. 9(f). Figures 9(g)-9(i) further reveal that increasing temperature led to a substantial increase in cavity expansion, crack propagation, and porosity change. For example, the results indicated that as the temperature increased from 170 to 230 °C, cavity expansion increased by up to 106%, and porosity change increased by up to 58%. The ANOVA confirmed the significance of temperature in the cavity expansion (p-value = 0.000), crack propagation (p-value = 0.000), and porosity change (p-value = 0.000).

The effect of temperature on defect generation can be partially attributed to changes in the properties of the binder, as depicted in Fig. 11. At lower temperatures, the binder exhibited higher elasticity, enabling greater initial cavity expansion when gas was injected into the cavity. Upon the release of gas pressure, this increased elasticity allowed the cavity to spring back with minimal plastic deformation. In contrast, at higher temperatures, the binder stiffened and weakened, leading to reduced initial expansion and an increased likelihood of crack propagation when gas was injected. Despite the reduction in initial expansion, the enhanced stiffness of the binder hindered the cavity from returning to its original state after the release of gas pressure, resulting & in higher permanent expansion. Another factor to take into one account regarding the influence of temperature is its impact on the interface properties. While this aspect was not examined in this study, future research is necessary to explore how temperature affects bonding mechanisms.

E. Influence of compaction pressure

The scanned images shown in Figs. 10(a)-10(f) present the influence of compaction pressure on defect generation in the samples. In the sample fabricated with a lower compaction pressure (0 and 5 MPa), the cracks tended to remain around the cavity. In contrast, in the samples fabricated with a higher compaction pressure (10 MPa), the cracks propagated through the entire sample.

The results in Fig. 10(g) show that the effect of compaction expansion was insignificant pressure on the cavity (p-value = 0.156), particularly when the applied gas pressure was low (i.e., 4.13 or 5.51 MPa). This can be attributed to the interplay of two competing effects of compaction pressure on cavity expansion: gas escaping and strength change. When the injected gas pressure was low (i.e., 4.13 or 5.51 MPa), both effects of gas escaping and strength change came into play. That is, as the compaction pressure decreased from 10 to 0 MPa, the sample's porosity increased, while its elasticity increased and yield strength decreased, as indicated in our previous research.³¹ The higher porosity allowed the gas to escape more easily from the sample, resulting in lower cavity expansion. Conversely, the higher elasticity and lower yield strength contributed to higher cavity expansion. As a result, these effects counterbalance each other, leading to an overall

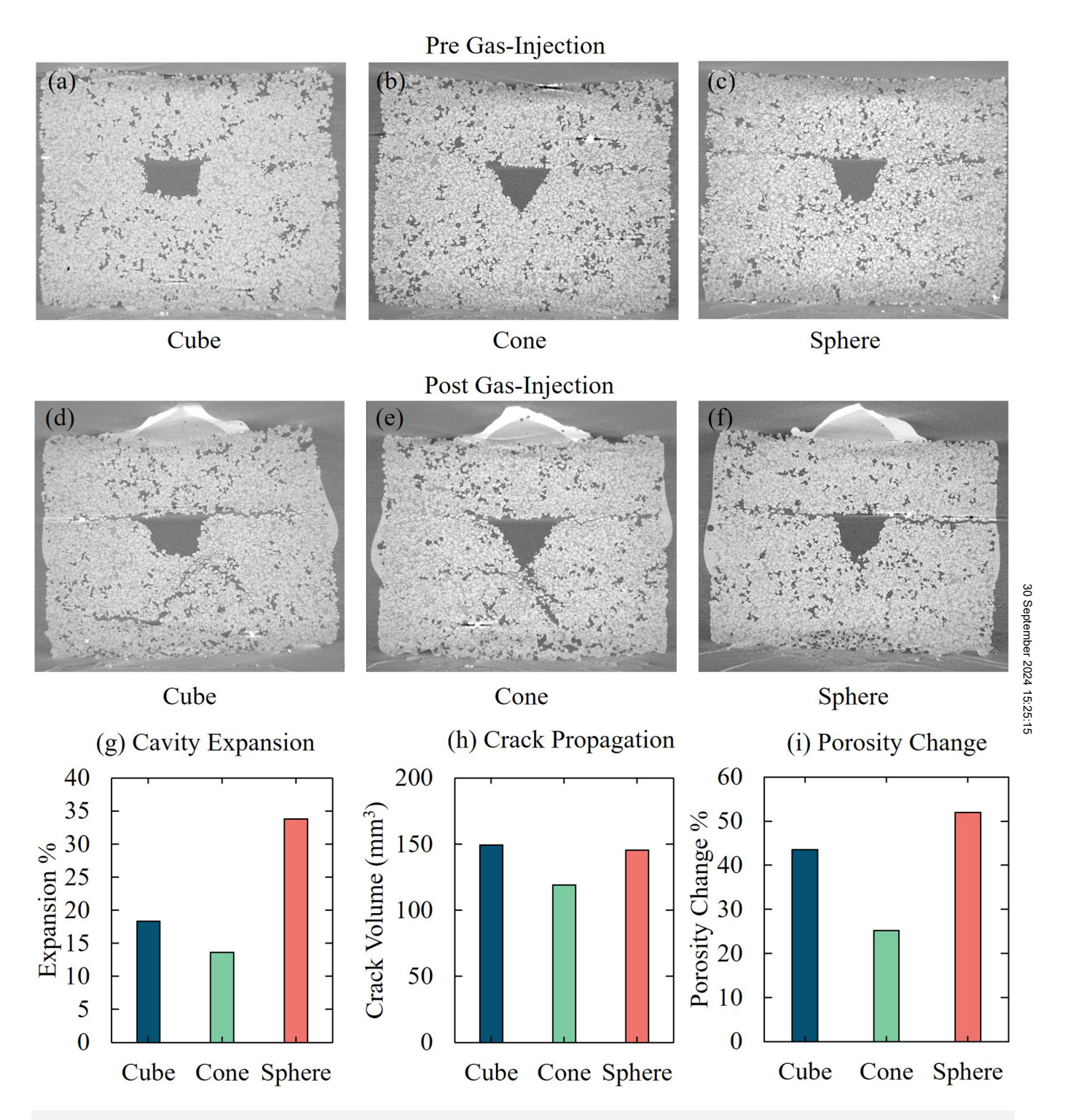


FIG. 8. Micro-CT scans of samples (a)-(c) before gas injection and (d)-(f) after gas injection. Effect of cavity shape on (g) cavity expansion, (h) crack propagation, and (i) porosity change.

FIG. 9. Micro-CT scans of samples (a)–(c) before gas injection and (d)–(f) after gas injection. Red arrows indicate initial point of failure within the cavity. Effect of temperature on (g) cavity expansion, (h) crack propagation, and (i) porosity change.

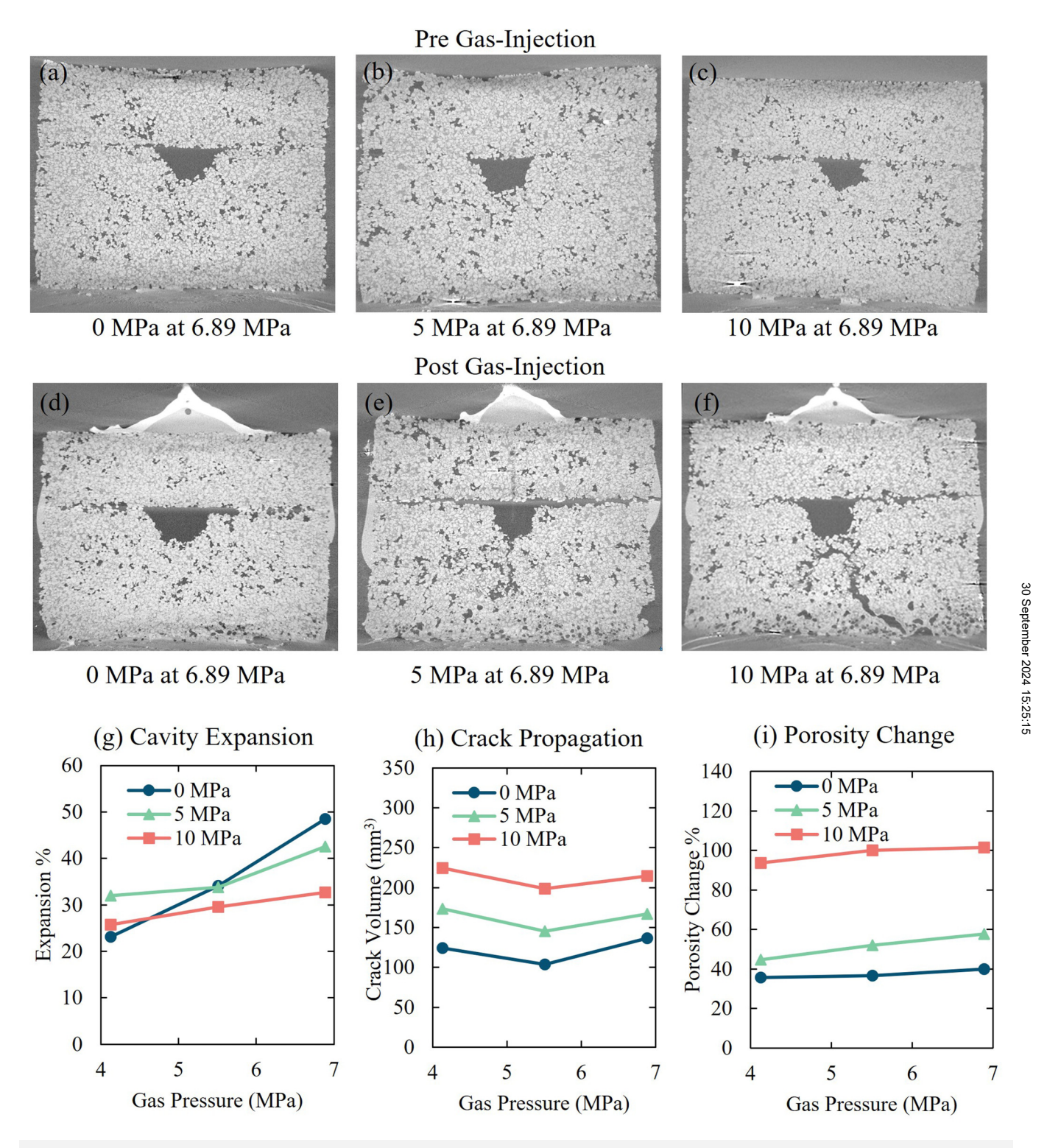


FIG. 10. Micro-CT scans of samples (a)–(c) before gas injection and (d)–(f) after gas injection. Effect of compaction pressure on (g) cavity expansion, (h) crack propagation, and (i) porosity change.

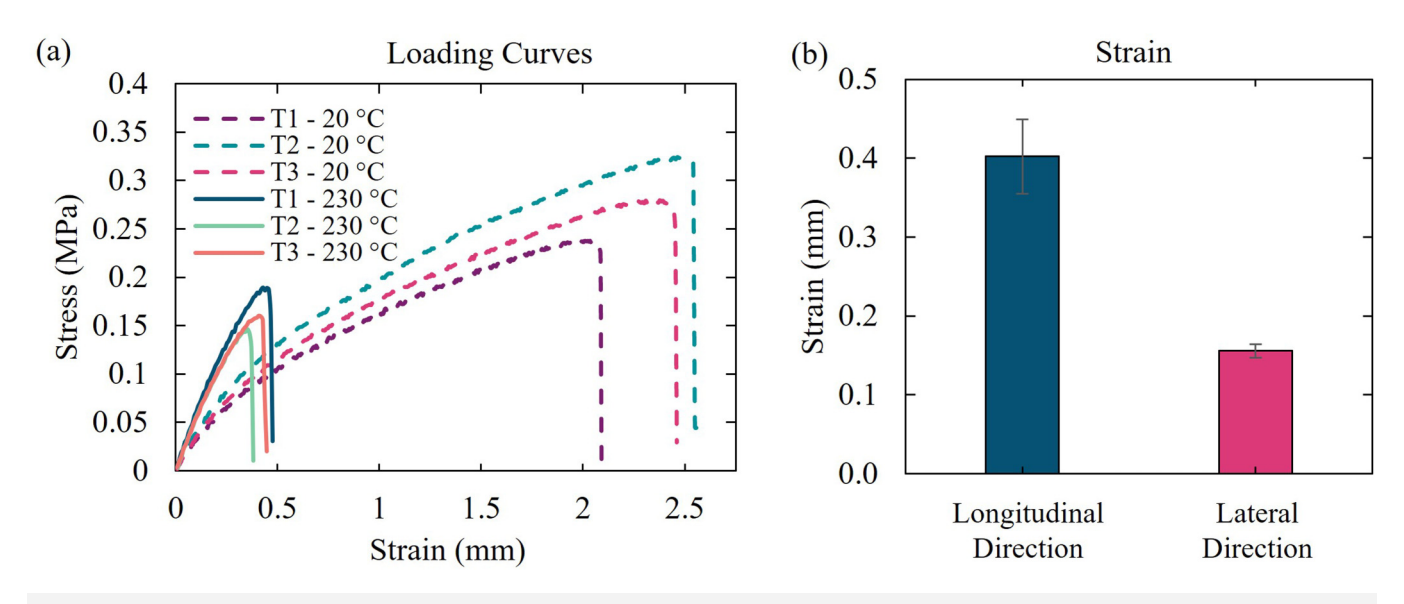


FIG. 11. Results from binder tensile testing including (a) loading curves of 20 and 230 °C and (b) longitudinal and lateral strains.

non-significant change in cavity expansion. On the other hand, when the gas pressure was high (e.g., 6.89 MPa), the gas could not escape easily from the sample, regardless of its porosity. Consequently, the gas escaping effect became less dominant, while the strength change effect became more prominent. This led to higher cavity expansion at lower compaction pressures.

Figures 10(h) and 10(i) indicate that compaction pressure has a significant influence on crack propagation (p-value = 0.001) and porosity change (p-value = 0.000). The results show that higher compaction pressure resulted in higher porosity change, especially in the form of crack propagation. When the compaction pressure was lower, the sample tended to have higher porosity. In this case, when subjected to internal gas injection, the pores provided pathways for the gas to be released, reducing the likelihood of major crack formation. The gas pressure was effectively released through these existing pathways. On the other hand, the samples fabricated with higher compaction pressure exhibited higher brittleness,3 resulting in more significant cracks compared to samples with lower compaction pressure.

Based on the findings, it can be concluded that higher gas pressure and lower compaction pressure are desirable for maximizing cavity expansion as they minimize the gas escaping effect and promote greater deformation due to increased elasticity and decreased yield strength. Conversely, higher compaction pressure is preferred for maximizing crack propagation as it results in a denser and stronger material that becomes more brittle, facilitating more pronounced crack initiation and propagation under stress.

F. Simulation of defect generation

1. Binder properties

Figure 11(a) illustrates the loading curves obtained from the binder tensile tests conducted at different temperatures.

Figure 11(b) displays the longitudinal and lateral strain data obtained from the binder test conducted under 230 °C. Three samples were tested at room temperature (20 °C) as a baseline, and another set of three samples were tested at 230 °C to simulate the another set of three samples were tested at 230 °C to simulate the thermite burning temperature experienced in real-world application. The results reveal that as the temperature increased, the samples exhibited a stiffer behavior but with reduced strength. The samples exhibited a stiffer behavior but with reduced strength. The stress required for yield or fracturing almost doubled for the room temperature sample compared to the sample tested at the elevated of temperature. The material properties of the sample at 230 °C were calculated from the loading curves as well as the longitudinal and on lateral strain data. The results are listed in Table III and were used in the composite simulation.

2. Simulation of gas pressure

The composite simulation results for different pressures (1, 5, 7, and 7.5 MPa) are presented in Figs. 12(a)-12(d). Under a

TABLE III. Binder properties obtained from the tensile tests for FEA simulation.

Material properties						
HTPB binder						
Young's modulus (MPa)	Poisson's ratio					
42.79	0.3963					
Fracture strain	Stress triaxiality	Damage evolution				
0.1848	0.333	0.0603				
Yield stress (MPa)						
0.1, 2.86, 5.86, 8.11, 10.36, 12.28, 14.2, 15.53						
Plastic strain						
0, 0.05, 0.1, 0.15, 0.2, 0.25, 0.3, 0.35						

pressure of 1 MPa [Fig. 12(a)], the stress on the cavity surface is minimal, resulting in limited deformation. Delamination, which refers to the separation between the particles and the surrounding binder, was not observed at this low pressure.

As the pressure increased to 5 MPa [Fig. 12(b)], the stress on the binder quadrupled, leading to expansion of the surrounding binder. The binder at the surface of the particles experienced varying levels of strain due to differences in thickness. This discrepancy in strain initiated delamination specifically at certain corners of the particle-binder interface and caused slight movement of the particles. The cavity deformation was significant, but no fracture occurred in the binder phase of the mock PBX.

At a pressure of 7 MPa [Fig. 12(c)], the stress on the binder increased by over 40%, resulting in further expansion. The elevated stress and strain levels led to a significant increase in

delamination, particularly at the particle corners. The increased severity of delamination promoted the onset of fracture in the binder. Some sharp particle corners had greater displacement than others, causing more pronounced delamination compared to the surrounding regions. The thinnest regions of the binder underwent the highest stress concentrations where the particles exhibited sharp corners. These regions with less binder acted as weak points in the composite. As the particles shifted and delamination propagated, the weak binder regions broke through to the particles. Fracture occurred at these points, amplifying the delamination post-fracture. The fractured regions provided greater movement for the particle, resulting in more substantial separation.

In the simulation conducted at a pressure of 7.5 MPa [Fig. 12(d)], an extra fracture point emerged in the binder phase in comparison

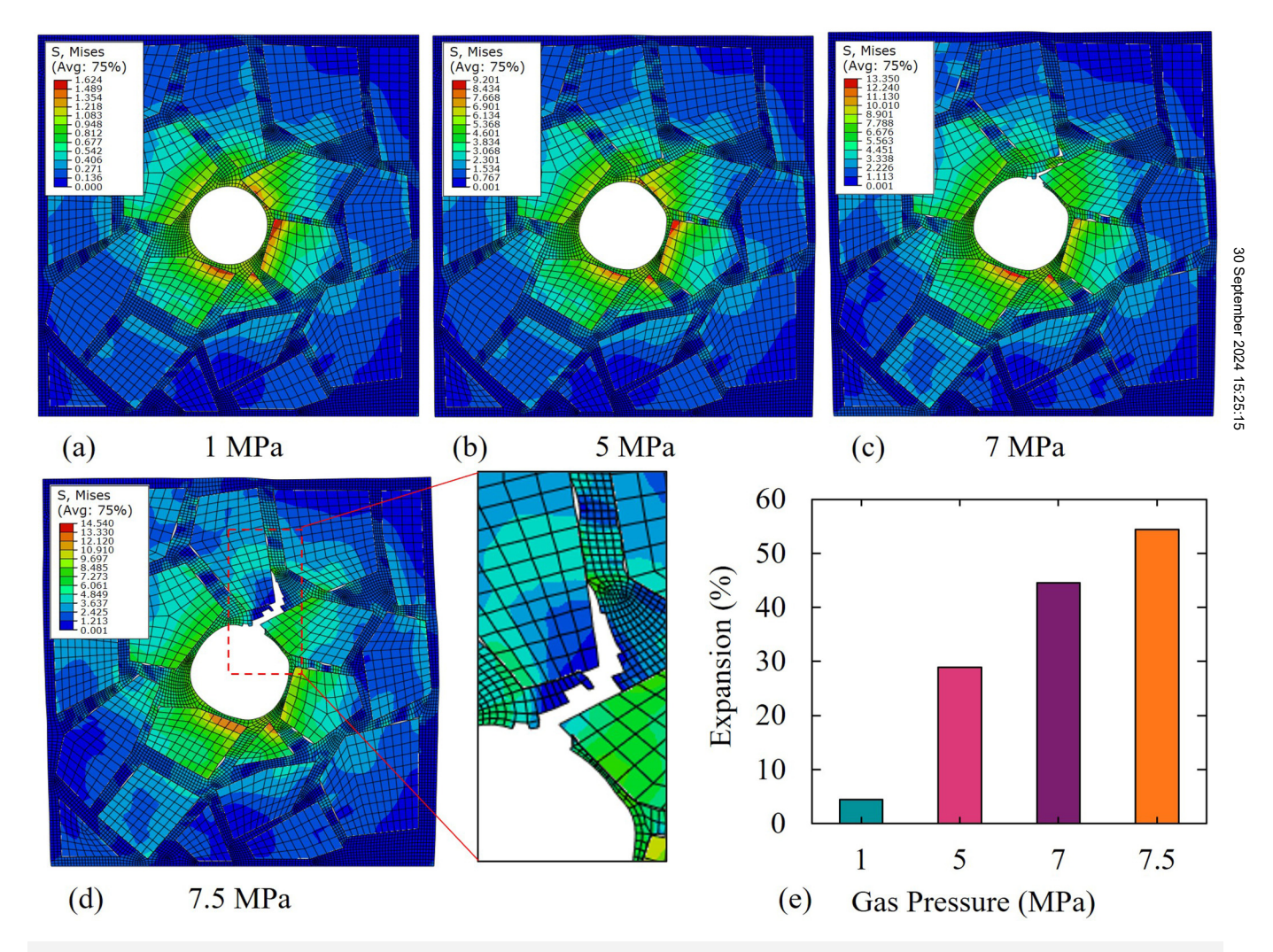


FIG. 12. Von Mises stresses (MPa) for four levels of pressure including (a) 1, (b) 5, (c) 7, and (d) 7.5 MPa. (e) Cavity expansion for different gas pressures.

to the results obtained under 7 MPa. As the fracture propagated throughout the binder between the adjacent particles, stress concentrations accumulated at the nearest binder-particle interface, resulting in further delamination. Similar to the initial fracture crack, the subsequent crack occurred at a thinner region of the binder and a sharp particle corner. This fracture point exhibited similar behavior, with magnified delamination due to the additional movement of particles. Overall, these results are consistent with experimental observations where significant fracture beyond the corners of a sphere cavity typically began near 7 MPa. The absence of fracture under lower pressure can be attributed to

differences in cavity shape. That is, the simulation considered a complete sphere with uniform stress distribution, whereas the experimental setup employed a half sphere, resulting in weakened points at the corners.

The expansion of the cavity was quantified in Fig. 12(e). The simulation at 1 MPa showed minimal expansion. As the pressure increased, the expansion became more significant. The cavity expanded by approximately 10% between 5 and 7 MPa, and up to a 54.4% increase was observed at 7.5 MPa. These results provide valuable insights into the effect of pressure on cavity expansion, delamination, and damage within the composite simulation.

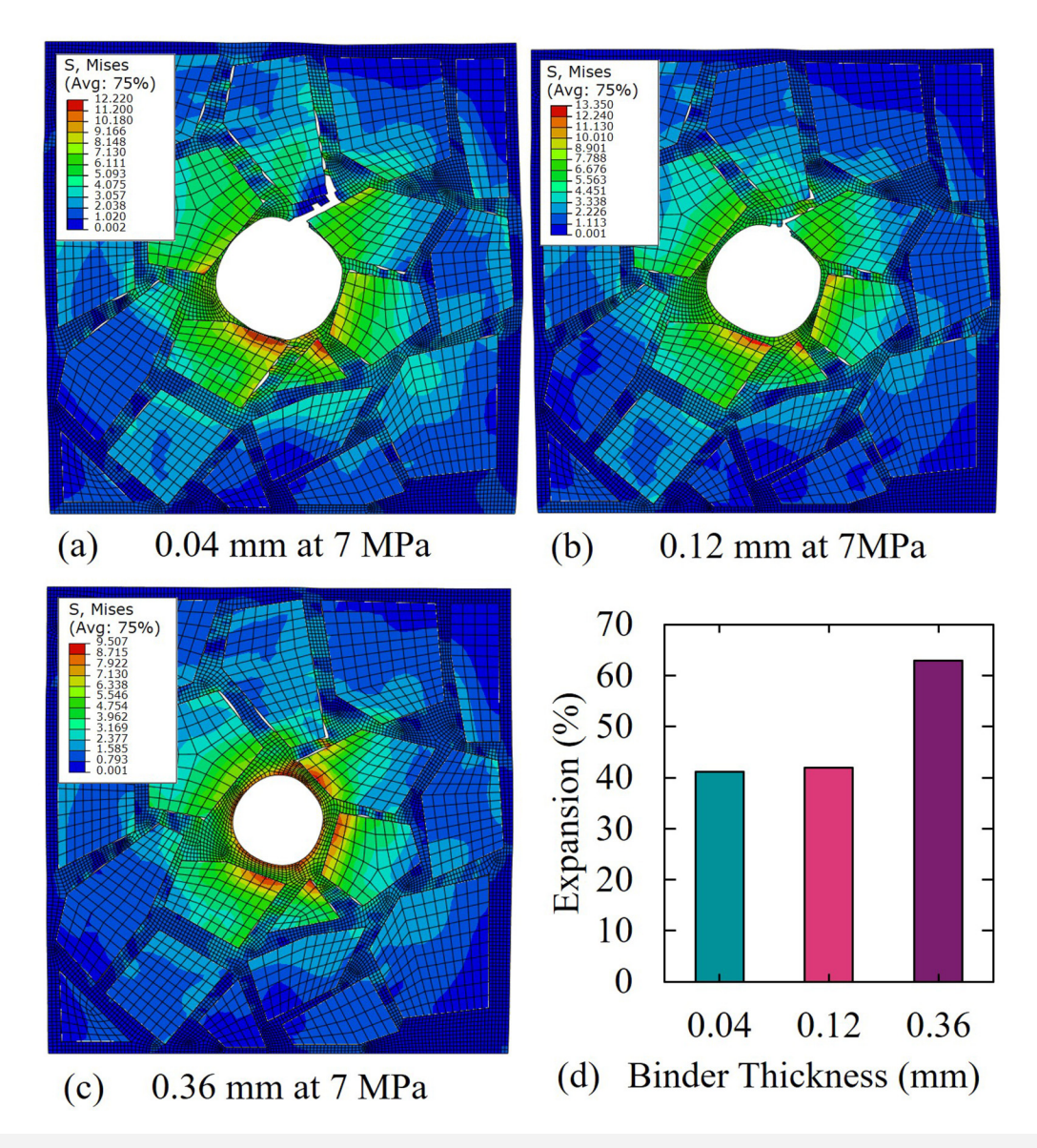


FIG. 13. von Mises stresses (MPa) for three levels of binder thickness expressing the binder thickness including (a) 0.04, (b) 0.12, and (c) 0.36 mm. (e) Mapped cavity expansion.

3. Simulation of binder thickness

The simulation results for different binder thicknesses around the cavity, representing a change in solids loading, are presented in Fig. 13. The property replicates the change in compaction pressure, also influencing the solids loading. Under the lowest binder thickness [Fig. 13(a)], the most significant degree of fracture was observed. Thinner regions of binder provided a weaker cavity, making it easier to initiate fracture. The entire cavity expanded further, leading to a second fracture progressing further from the first fracture. In the second case [Fig. 13(b)], where the binder thickness was slightly increased, the fracture was less dramatic, but the binder was still weak enough to experience damage. In the last case [Fig. 13(c)] with the thickest binder, no fracture occurred. The thicker binder provided a more uniform distribution of stress because the cavity was less affected by particle movements.

Moreover, the thicker region required a higher level of stress to initiate damage. These results clearly demonstrate the influence of solids loading on PBX fracture. A higher solids loading, represented by thinner binder thickness, increases the likelihood of fracture occurrence. Thicker binder, on the other hand, reduces the probability of fracture due to its higher strength and more uniform stress distribution.

The results for cavity expansion [Fig. 13(d)] indicate that while the cracking was most severe under the thinnest binder thickness [0.04 mm, Fig. 13(a)], the expansion of the cavity was the least in this case. Conversely, the greatest expansion was observed under the thickest binder thickness [0.36 mm, Fig. 13(c)]. The higher amount of binder allows for more expansion without being influenced by the particles. In alignment with the experimental results, a higher solids loading provides greater porosity change.

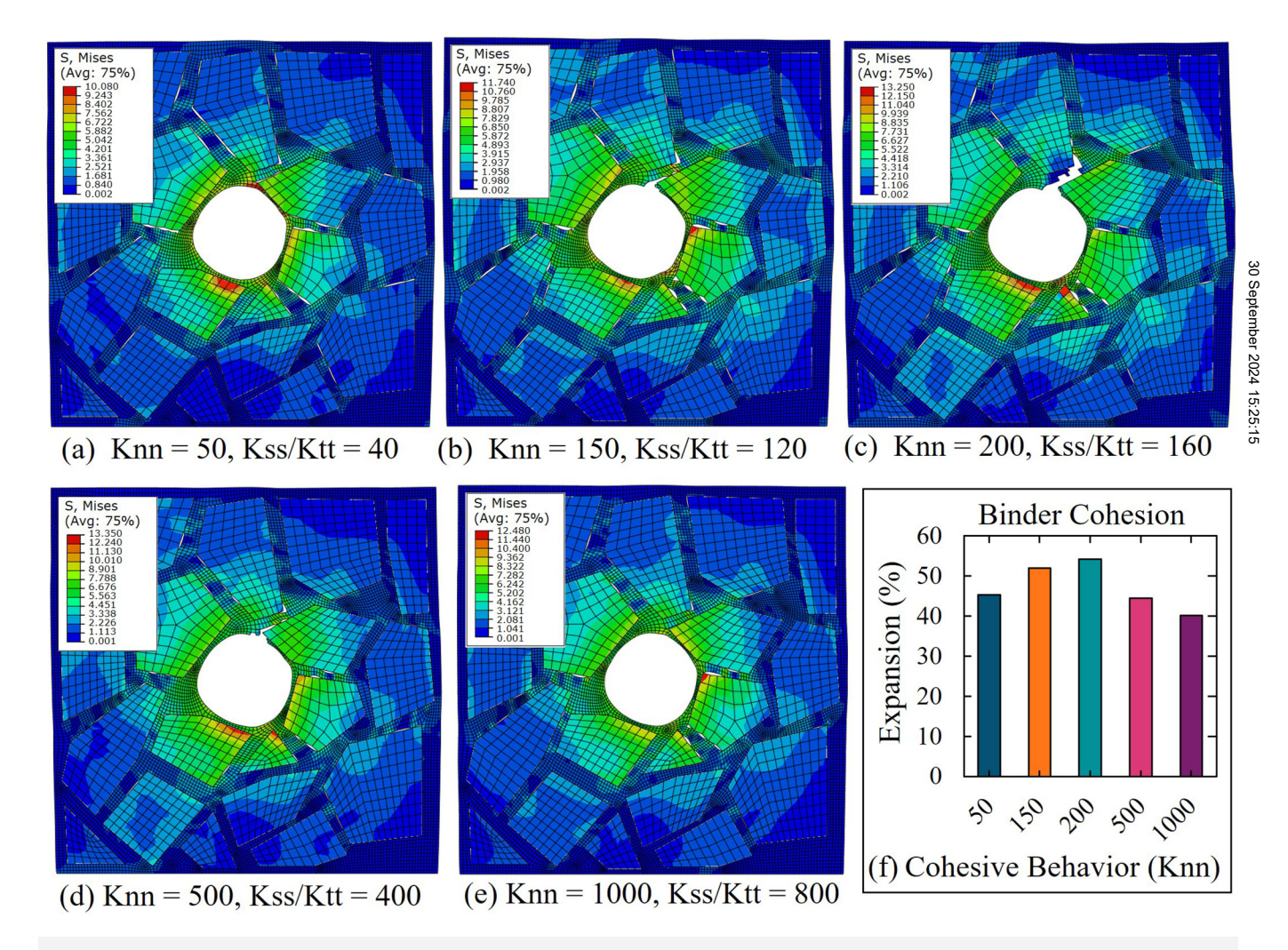


FIG. 14. von Mises stresses (MPa) for five levels of cohesive behavior including (a) $K_{nn} = 50$, $K_{ss}/K_{tt} = 40$, (b) $K_{nn} = 150$, $K_{ss}/K_{tt} = 120$, (c) $K_{nn} = 200$, $K_{ss}/K_{tt} = 160$, (d) $K_{nn} = 500$, $K_{ss}/K_{tt} = 400$, and (e) $K_{nn} = 1000$, $K_{ss}/K_{tt} = 800$. (f) Mapped cavity expansion.

4. Simulation of interface properties

The simulation results for different levels of cohesion properties at 7 MPa are presented in Fig. 14. In the case of lower cohesion values [Fig. 14(a)], indicating poor binder adhesion at the particle interface, significant delamination occurs, but no fracture is observed. The lack of adhesion allows for greater movement of particles and binder, facilitating stress release and preventing fracture

As the cohesion properties increase [Figs. 14(b) and 14(c)], delamination occurs at fewer interfaces, leading to a higher level of stress concentration in regions where interfaces are strongly bonded, leading to a higher level of stress concentration. This concentration of stress enables fracture initiation in both cases, with the higher cohesion properties [Fig. 14(c)] resulting in more dramatic fracture. However, as the cohesion properties continue to increase [Figs. 14(d) and 14(e)], the trend reverses. Delamination starts to decrease, and fracture eventually discontinues. Higher cohesion causes the composite to act more cohesively, and fracture becomes less likely under the applied pressure. These results highlight the importance of binder properties, specifically adhesion, in PBX fracture behavior. If the adhesion is too low, the composite struggles to fracture due to more interface delamination and enhanced stress release. On the other hand, if the binder adheres too strongly to the particles, fracture is also hindered due to enhanced interface bonding. A balance is required in the adhesive properties of the binder for optimal fracture behavior.

The results for cavity expansion [Fig. 14(f)] demonstrate that at a pressure of 7 MPa, all cohesion property values resulted in over 40% expansion. The results follow a bell-curve relationship, with the maximum expansion of approximately 54.3% achieved at a cohesion property value of $K_{nn} = 200$ and $K_{ss}/K_{tt} = 160$. These properties can be utilized in conjunction with pressure to target a specific pore size during expansion, allowing for more precise control over the expansion process.

It is worth noting that the crack propagation generated in the simulation (Figs. 12-14) is not as dramatic as observed in the experiments. This discrepancy can be attributed to the simplified boundary conditions and gas pressure applied in the simulation. Specifically, in the simulation, pressure was applied only at the edge of the inner cavity, whereas in the experiments, gas pressure was transferred through the delaminated interfaces and cracks, leading to more extensive damage.

IV. CONCLUSIONS

The study presented a comprehensive framework for characterizing the defect generation process induced by internal gas pressure in PBXs. By employing both experimental and numerical methods, the relationship between different processing parameters and generated defects was mapped. In the experimental study, mock PBX samples were created with cavities, and gas was injected into these cavities. X-ray micro-CT imaging was utilized to analyze the microstructure of the samples before and after gas injection. The results showed that higher gas pressure and temperature led to greater defect generation (i.e., cavity expansion, crack propagation, and porosity change), while compaction pressure had more significant effects on crack propagation and porosity change. In addition, it was observed that a spherical cavity resulted in more defect generation, while a conical cavity allowed for location-controlled crack

The findings were further expanded using cohesive finite element analysis. Custom binder properties were obtained through mechanical testing, and these properties were validated by comparing the results with experimental tests. The properties were then incorporated into a composite simulation, which captured the interaction between the binder and particles, as well as the cavity expansion during thermite ignition. The simulation revealed that gas pressure had a significant influence, leading to cavity expansion of up to 54%. It also provided insights into binder failure, indicating when and where fracture is likely to occur. The cohesive properties of the binder demonstrated a bell-curve relationship between adhesion level and resulting fracture behavior. Additionally, altering the cavity size demonstrated that thicker regions of binder were more resistant to fracture but resulted in greater expansion, while thinner regions were more prone to fracture but exhibited limited

While this study was conducted using mock PBXs with lower solids loading and smaller specimen sizes than actual PBXs, the insights gained offer valuable guidance for designing and producing thermite inclusions and PBX materials for the controlled generation of defects. Future research should aim to investigate defect generation in those material configurations (e.g., >95 wt. % solids loading and centimeter sizes) at the scale relevant to real-world applications.

ACKNOWLEDGMENTS

(NOWLEDGMENTS

The authors would like to acknowledge the support from the U.S. Air Force Office of Scientific Research under Grant No. 8 FA9550-20-1-0700 (Program Officer: Martin Schmidt and Chiping Li). H.S.U. and X.S. would also like to acknowledge the support from the U.S. National Science Foundation under Grant No. 3 2118393.

AUTHOR DECLARATIONS

Conflict of Interest

The authors have no conflicts to disclose.

Author Contributions

Levi Kirby: Formal analysis (lead); Investigation (lead); Methodology (equal); Validation (equal); Visualization (equal); Writing - original draft (lead). Travis Sippel: Funding acquisition (equal); Investigation (supporting). H. S. Udaykumar: Funding acquisition (equal); Investigation (supporting); Writing - review & editing (supporting). Xuan Song: Conceptualization (lead); Formal analysis (supporting); Funding acquisition (equal); Investigation (supporting); Methodology (equal); Project administration (equal); Supervision (lead); Writing – review & editing (lead).

DATA AVAILABILITY

The data that support the findings of this study are available from the corresponding author upon reasonable request.

REFERENCES

- ¹K. Yang, Y. Wu, and F. Huang, Eur. J. Mech. A/Solids 80, 103924 (2020).
- ²Y. Wei, S. Kim, Y. Horie, and M. Zhou, J. Appl. Phys. 124, 165110 (2018).
- ³T. M. Willey, T. Van Buuren, J. R. Lee, G. E. Overturf, J. H. Kinney, J. Handly, B. L. Weeks, and J. Ilavsky, Propellants, Explos., Pyrotech. 31, 466 (2006).
- ⁴S. Roy, B. P. Johnson, X. Zhou, Y. T. Nguyen, D. D. Dlott, and H. Udaykumar, J. Appl. Phys. **131**, 205901 (2022).
- ⁵Z. L. Bai, Z. P. Duan, X. J. Wang, and F. L. Huang, Propellants, Explos., Pyrotech. 46, 1723 (2021).
- ⁶Q. An, W. A. Goddard III, S. V. Zybin, A. Jaramillo-Botero, and T. Zhou, J. Phys. Chem. C 117, 26551 (2013).
- ⁷S. Kim, A. Barua, Y. Horie, and M. Zhou, J. Appl. Phys. 115, 174902 (2014).
- ⁸K. Yang, Y. Wu, and F. Huang, Mech. Mater. 137, 103130 (2019).
- ⁹K. Zhong, R. Bu, F. Jiao, G. Liu, and C. Zhang, Chem. Eng. J. **429**, 132310 (2022).
- ¹⁰C. Coffelt, D. Olsen, C. Miller, and M. Zhou, J. Appl. Phys. 131, 065101 (2022).
- ¹¹P. Das and H. Udaykumar, Shock Waves **32**, 593 (2022).
- ¹²H. K. Springer, S. Bastea, A. L. Nichols III, C. M. Tarver, and J. E. J. P. Reaugh, Propellants Explos. Pyrotech. 43, 805 (2018).
- ¹³C. B. Brown, A. H. Mueller, S. Sridhar, J. P. Lichthardt, A. M. Schmalzer, B. C. Tappan, V. H. Whitley, L. G. Hill, E. Lozano, and T. D. Aslam, Phys. Rev. Lett. 130, 116105 (2023).
- ¹⁴A. L. Higginbotham Duque, W. L. Perry, and C. M. Anderson-Cook, Propellants, Explos., Pyrotech. 39, 275 (2014).
- ¹⁵W. L. Perry, B. Clements, X. Ma, and J. T. Mang, Combust. Flame 190, 171 (2018).

- ¹⁶N. K. Rai, W. L. Perry, and A. L. Duque, J. Appl. Phys. 131, 175105 (2022).
- 17A. Lawrence and T. Sippel, in Remotely Induced Porosity Using Microwave Absorptive Inclusions, (AIAA, 2022), p. 0573.
- ¹⁸S. J. Barkley, A. R. Lawrence, M. Zohair, O. L. Smithhisler, C. L. Pint, J. B. Michael, and T. R. Sippel, Appl. Mater. Interfaces 13, 39678 (2021).
- ¹⁹E. E. Iglesias, T. Rowe, K. Fernandez, S. Chocron, and J. Wilkerson, J. Compos. Mater. 55, 2577 (2021).
- ²⁰L. Kirby, A. Lawrence, H. S. Udaykumar, T. Sippel, and X. Song, Addit. Manuf. 77, 103808 (2023).
- ²¹H. Naseem, J. Yerra, H. Murthy, and P. Ramakrishna, Energ. Mater. Front. 2, 111 (2021).
- **22**Y. Lou and H. Huh, Int. J. Solids Struct. **50**, 447 (2013).
- 23T. Feng, J.-S. Xu, L. Han, and X. Chen, Modeling and Simulation of the Debonding Process of Composite Solid Propellants (IOP Publishing, 2017), p. 012020.
- p. 012020.

 24D. J. Walters, D. J. Luscher, J. D. Yeager, and B. M. Patterson, Int. J. Mech. Sci. 140, 151 (2018).
- ²⁵H. Arora, E. Tarleton, J. Li-Mayer, M. Charalambides, and D. Lewis, Comput. Mater. Sci. 110, 91 (2015).
- ²⁶D. S. Dugdale, J. Mech. Phys. Solids **8**, 100 (1960).
- ²⁷G. I. Barenblatt, J. Appl. Math. Mech. 23, 622 (1959).
- ²⁸R. Hu, C. Prakash, V. Tomar, M. Harr, I. E. Gunduz, and C. Oskay, Int. J. Fract. **203**, 277 (2017).
- ²⁹See https://www.minitab.com for "Minitab" (2021).
- ³⁰C. J. Wu and M. S. Hamada, Experiments: Planning, Analysis, and Optimization (John Wiley & Sons, 2011).
- ³¹L. Kirby, F. Fei, and X. Song, Powder Technol. **415**, 118146 (2022).